Interactions between Boreal Summer Intraseasonal Oscillations and Synoptic-Scale Disturbances over the Western North Pacific. Part II: Apparent Heat and Moisture Sources and Eddy Momentum Transport*

PANG-CHI HSU AND TIM LI

International Pacific Research Center, and School of Ocean and Earth Science and Technology, University of Hawaii at Manoa, Honolulu, Hawaii

(Manuscript received 7 May 2010, in final form 23 August 2010)

ABSTRACT

The interactions between the boreal summer intraseasonal oscillation (ISO) and synoptic-scale variability (SSV) are investigated by diagnosing the atmospheric apparent heat source (Q_1), apparent moisture sink (Q_2), and eddy momentum transport. It is found that the synoptic Q_1 and Q_2 heating (cooling) anomalies are in phase with cyclonic (anticyclonic) vorticity disturbances, aligned in a southeast–northwest-oriented wave train pattern over the western North Pacific (WNP). The wave train is well organized and strengthened (loosely organized and weakened) during the ISO active (suppressed) phase. The nonlinearly rectified Q_1 and Q_2 fields due to the eddy–mean flow interaction account for 10%–30% of the total intraseasonal Q_1 and Q_2 variabilities over the WNP. During the ISO active (suppressed) phase, the nonlinearly rectified intraseasonal Q_1 and Q_2 heating (cooling) appear to the northwest of the ISO enhanced (suppressed) convection center, favoring the northwestward propagation of the ISO. A diagnosis of the zonal momentum budget shows that the eddy momentum flux convergence forces an intraseasonal westerly (easterly) tendency to the north of the ISO westerly (easterly) center during the ISO active (suppressed) phase. As a result, the eddy momentum transport may contribute to the northward propagation of the boreal summer ISO over the WNP.

1. Introduction

Both the intraseasonal oscillation (ISO) and the synoptic-scale variability (SSV) are vigorous over the western North Pacific (WNP) in the boreal summer. In Hsu et al. (2011, hereafter Part I), we investigated the interaction between the ISO and SSV from the energetics point of view. It was found that during the ISO active (suppressed) phase, the synoptic-scale eddy gains (loses) kinetic energy from (to) the ISO and both the cyclonic and convergent components of the ISO flows play a role in the barotropic energy conversion. In addition to the barotropic energy conversion, the eddy geopotential flux convergence, which is partly related to diabatic heating, also accounts for the intraseasonal EKE variability. In the second part of this study, the characteristics and mechanisms associated with the SSV–ISO interactions will be further examined based on the diagnoses of the atmospheric apparent heat source (Q_1), apparent moisture sink (Q_2), and eddy momentum transport.

Whereas the boreal winter ISO is characterized by the pronounced equatorial-trapped eastward-propagating Madden–Julian oscillation (MJO; Madden and Julian 1971), the boreal summer ISO shows prominent northward- and northwestward-propagating features over the WNP (e.g., Wang and Rui 1990; Kawamura et al. 1996; Wang and Xie 1997; Hsu and Weng 2001; Kemball-Cook and Wang 2001; Tsou et al. 2005). The WNP summer ISO is characterized by deep convection coupled with large-scale cyclonic vorticity anomalies. Both the internal atmospheric dynamics and air–sea interactions may be responsible for the northwestward propagation of the ISO. Based on the simulation of an intermediate atmospheric model, Wang and Xie (1997) suggested that the emanation of Rossby waves is responsible for the northwestward propagation. Observational studies showed that the atmospheric vorticity and boundary layer convergence

* School of Ocean and Earth Science and Technology Contribution Number 8023 and International Pacific Research Center Contribution Number 723.

Corresponding author address: Tim Li, IPRC, SOEST, University of Hawaii at Manoa, 1680 East–West Road, POST Bldg. 401, Honolulu, HI 96822.
E-mail: timli@hawaii.edu

DOI: 10.1175/2010JCLI3834.1

lead the ISO convection (Kawamura et al. 1996; Hsu and Weng 2001). The leading of the vorticity is attributed to the interaction of the ISO flow with the background easterly vertical shear (Jiang et al. 2004). The latent heating induced by the boundary layer moisture convergence may further cause the northwestward shift of the ISO convection (Hsu and Weng 2001; Jiang et al. 2004). Tsou et al. (2005) pointed out that the northwestward-propagating ISO results from the combined effects of vorticity advection and surface frictional-induced diabatic heating. Kemball-Cook and Wang (2001) and Fu et al. (2003) suggested that the air–sea interaction may contribute to the ISO propagation.

The dominant mode of SSV in the boreal summer over the WNP is a northwest–southeast-oriented wave train with a wavelength of near 3000 km and a period of 3–10 days (Lau and Lau 1990; Chang et al. 1996; Li 2006; Tam and Li 2006). The origin of the synoptic wave train arises from the instability of the summer mean flow in the presence of the convection–circulation feedback (Li 2006). However, how the summertime synoptic-scale eddy feeds back to the ISO is not clear. Matthews and Kiladis (1999) and Straub and Kiladis (2003) studied the interaction of the extratropical transient eddy with the boreal winter MJO, and suggested that the high-frequency convective activity embedded in the low-frequency MJO is responsible for the development of both the MJO and the eddy. Based on a theoretical model, Biello and Majda (2005), Biello et al. (2007), and Majda and Stechmann (2009) suggested that the synoptic-scale momentum and temperature flux convergences may modulate the large-scale MJO circulation. Maloney (2009) suggested that the tropical synoptic-scale eddy plays a role in regulating the MJO activity during the boreal winter. Zhou and Li (2010) noted that a large portion of the tropical intraseasonal surface latent heat flux (LHF) comes from the contribution of SSV and that the nonlinearly rectified LHF induced by the synoptic eddy may contribute to the development and propagation of the summertime ISO over the WNP.

In this paper, we will examine the roles of nonlinear rectifications of the atmospheric apparent heat source (Q_1) and apparent moisture sink (Q_2) and eddy momentum transport in the upscale feedback, with an emphasis on their effects on the ISO propagation. The rest of this paper is organized as follows: section 2 describes the datasets and methods we adopted. The ISO modulations of the synoptic-scale Q_1 and Q_2 variabilities and the nonlinear rectifications of the intraseasonal Q_1 and Q_2 heating fields by SSV are examined in section 3. Section 4 focuses on the role of the eddy momentum transport in the ISO development and propagation. Section 5 summarizes the major results.

2. Data and methods

The primary datasets used in this part of this study include (i) the observed daily outgoing longwave radiation (OLR) from the National Oceanic and Atmospheric Administration (NOAA) polar-orbiting satellites (Liebmann and Smith 1996), (ii) the observed pentad precipitation from the Climate Prediction Center (CPC) Merged Analysis of Precipitation (CMAP) (Xie and Arkin 1997), (iii) the National Centers for Environmental Prediction/Department of Energy (NCEP–DOE) reanalysis (Kanamitsu et al. 2002), and (iv) the 40-yr European Centre for Medium-Range Weather Forecasts (ECMWF) Re-Analysis (ERA-40) (Uppala et al. 2005). The NCEP–DOE and ERA-40 products contain the zonal and meridional wind (u and v), vertical p velocity (ω), and temperature (T) fields at 17 levels from 1000 to 100 hPa. The specific humidity (q) field in the NCEP–DOE reanalysis has 8 levels from 1000 to 300 hPa, whereas it has 17 levels from 1000 to 100 hPa in the ERA-40. For the current analysis, we focus on the summer months from July to September, and the OLR, CMAP, and NCEP–DOE data from 1979 to 2007 and the ERA-40 data from 1979 to 2001 are used. All the datasets have a $2.5° \times 2.5°$ latitude–longitude grid.

To validate the reliability of Q_1/Q_2 calculations based on reanalysis, observed Q_1/Q_2 profiles from the Northern Enhanced Sounding Array (NESA) and the Southern Enhanced Sounding Array (SESA) of the South China Sea Monsoon Experiment (SCSMEX) are used. The rawinsonde-based estimates of Q_1/Q_2 are derived from the analyses of Johnson and Ciesielski (2002) for the intensive observing period (IOP) of 5 May–20 June 1998. Readers may refer to Johnson and Ciesielski (2002, their Fig. 1) for the rawinsonde sites associated with NESA and SESA.

The Butterworth bandpass filter (Hamming 1989) is used to derive the 10–90-day intraseasonal oscillation component, and a 10-day high-pass filter and a 90-day low-pass filter are used to obtain the synoptic-scale and low-frequency background state (LFBS) components, respectively. It is noted that the maximum variances of 10–90-day filtered 850-hPa vorticity fields derived from the NCEP–DOE and ERA-40 datasets appear in the same WNP region (20°–30°N, 125°–135°E). Therefore, an ISO index is constructed based on the 850-hPa vorticity time series over the maximum variance region. The ISO active and suppressed phases are defined when the 10–90-day vorticity time series exceeds one standard deviation. Based on this criterion, 224 (182) days and 199 (175) days are selected from the NCEP–DOE (ERA-40) reanalysis for ISO active and suppressed phase composites, respectively.

3. Contribution of SSV to intraseasonal apparent heat and moisture sources

According to Yanai et al. (1973), the atmospheric apparent heat source (Q_1) and apparent moisture sink (Q_2) may be computed as residuals of the thermodynamic and moisture equations, respectively:

$$Q_1 = c_p\frac{\partial T}{\partial t} - c_p(\omega\sigma - \mathbf{V}\cdot\nabla T), \quad (1)$$

$$Q_2 = -L\frac{\partial q}{\partial t} - L\mathbf{V}\cdot\nabla q - L\omega\frac{\partial q}{\partial p}, \quad (2)$$

where c_p denotes the specific heat at constant pressure, T the temperature, t the time, ω the vertical p velocity, $\sigma = (RT/c_pp) - (\partial T/\partial p)$ the static stability, R the gas constant, p the pressure, $\mathbf{V}$ the horizontal velocity vector, ∇ the horizontal gradient operator, L the latent heat of condensation, and q the specific humidity. Here Q_1 represents the total diabatic heating (including radiation, latent heating, and surface heat flux) and subgrid-scale heat flux convergences; Q_2, on the other hand, represents the latent heating due to condensation or evaporation processes and subgrid-scale moisture flux convergences (Yanai et al. 1973). Comparing the distributions of Q_1 and Q_2 may help discriminate specific heating processes in the atmosphere.

To examine the reliability of so-calculated Q_1 and Q_2 from the reanalysis data, we compare both the climatological summer [July–September (JAS)] mean and the intraseasonal variability of the Q_1 and Q_2 with observed CMAP precipitation fields. The overall spatial distributions and amplitudes of vertically averaged Q_1 and Q_2 calculated from the NCEP–DOE and ERA-40 data are similar to the heating rate converted from the CMAP precipitation (figure not shown). In addition, we validate the vertical profiles of the diagnosed heating fields against the Q_1 and Q_2 profiles derived from the NESA and SESA. The vertical–time sections of Q_1/Q_2 based on the SCSMEX NESA soundings and the two reanalysis datasets in the corresponding NESA domain are shown in Fig. 1. The vertical structure and evolution characteristics of Q_1 calculated from ERA-40 (Fig. 1c) and the NCEP–DOE (Fig. 1d) reanalysis are quite similar to the SCSMEX observation (Fig. 1a), with the maximum heating rate appearing in the mid–upper troposphere. The diagnosed Q_2 structure and evolution are also consistent with that observed, with a maximum heating rate appearing in a relatively low altitude (Figs. 1e–h). There is a slight underestimate of amplitude of the heating and cooling rates derived from the reanalysis products. The validation against the SCSMEX SESA Q_1/Q_2 profiles in general shows a similar result (figure not shown). These validations suggest that the diagnosed Q_1 and Q_2 fields based on the reanalysis products are reliable. Because of the similarity of the Q_1 and Q_2 fields derived from the NCEP–DOE and ERA-40 datasets, in the following only the averaged results are presented. As the moisture information in the NCEP–DOE reanalysis is available up to 300 hPa, the results of Q_2 above 300 hPa are solely based on ERA-40.

Before diagnosing the SSV–ISO interaction, we first conduct a spectrum analysis of Q_1 and Q_2 averaged over a large WNP domain (0°–35°N, 110°–170°E) during the boreal summer. The annual cycles of the Q_1 and Q_2 fields are subtracted before a fast Fourier transform (FFT) is applied. The spectrum analysis reveals that both the Q_1 and Q_2 fields have significant peaks at the intraseasonal (10–90 day) and synoptic-scale (<10 day) periods (Fig. 2). The two peaks are well above the red noise spectrum level. Therefore, it is reasonable to separate the LFBS, ISO, and SSV components in the Q_1 and Q_2 diagnoses. A careful examination of the synoptic spectrums of Q_1 and Q_2 indicates a peak at the period of 7 days for ERA-40 but 3–8 days for the NCEP reanalysis. The exact cause of the difference is not clear. It might be attributed to the model biases and resolutions and data assimilation methods used (Hodges et al. 2003; Marques et al. 2010).

Next we examine how ISO modulates the synoptic Q_1 and Q_2 in the WNP. Figure 3 shows the regressed Q_1 and Q_2 fields during the ISO active and suppressed phases. The regression is based on the 3–10-day vorticity time series averaged over a box region (20°–30°N, 125°–135°E) where the synoptic-scale variance is strongest. Figure 3 illustrates that a well-organized cyclonic–anticyclonic vorticity wave train appears during the ISO active phase. The synoptic wave train is oriented in the northwest–southeast direction (Fig. 3a), consistent with Lau and Lau (1990). Both the synoptic Q_1 and Q_2 fields are in phase with the vorticity field (Figs. 3a,c), with the low-level cyclonic (anticyclonic) vorticity collocated with the diabatic heating (cooling). The resemblances of the spatial distribution and amplitude of the vertically averaged Q_1 and Q_2 fields (Figs. 3a,c) suggest that the condensational heating is a major contributor to the diabatic processes. During the ISO suppressed phase, the synoptic wave train is much weaker and more loosely organized, even though the vorticity–heating phase relationship still exists (Figs. 3b,d). This implies that the activity of synoptic-scale disturbances is greatly modulated by the ISO, with a stronger (weaker) synoptic variability occurring during the ISO active (suppressed) phase, in agreement with results in Part I and previous studies (e.g., Maloney and Hartmann 2001; Maloney and Dickinson 2003; Straub and Kiladis 2003; Zhou and Li 2010). Mechanisms for the ISO modulations are through either the barotropic energy conversion

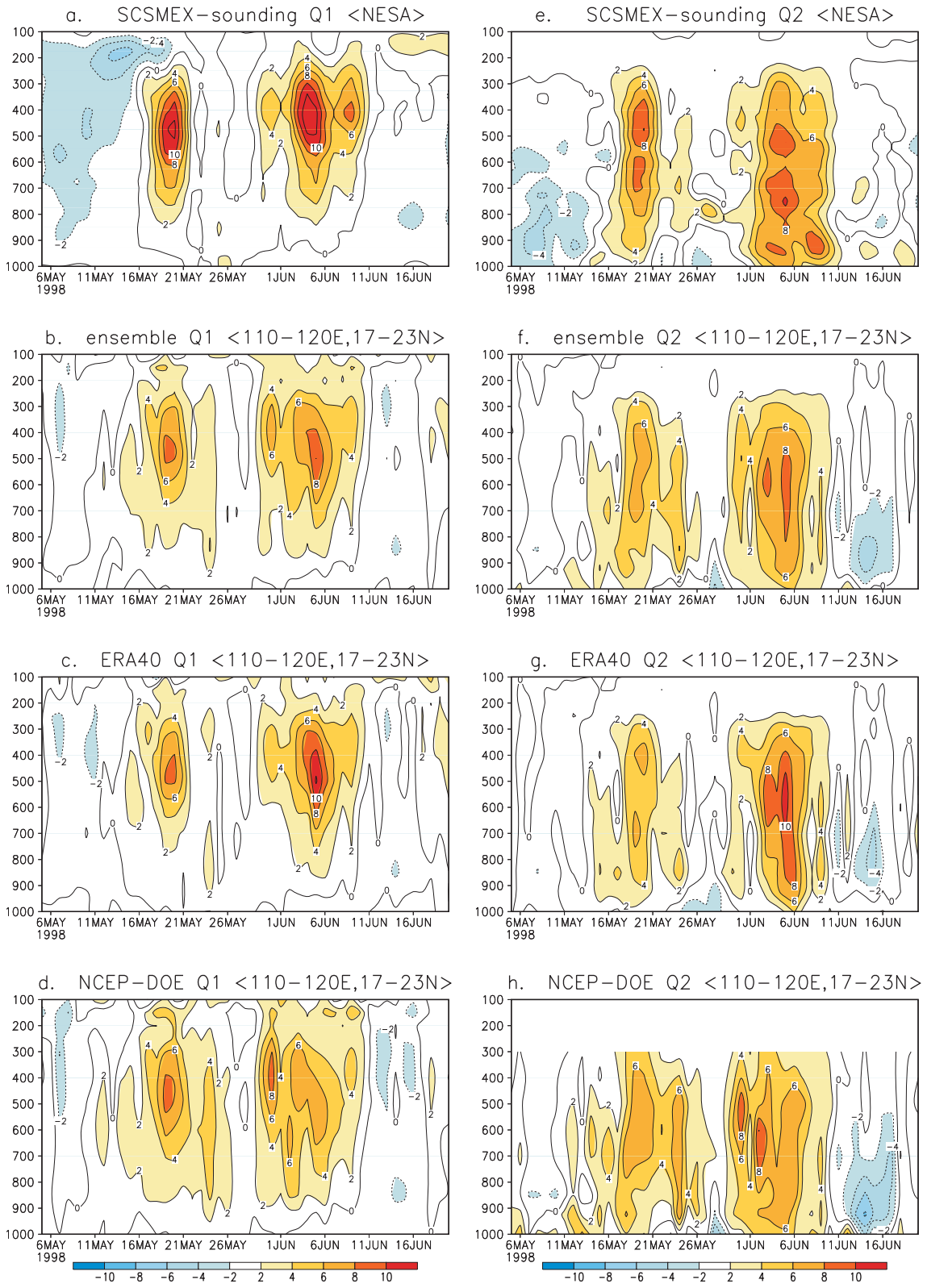

FIG. 1. The Q_1 profiles derived from (a) SCSMEX NESA rawinsonde, (b) average of ERA-40 and NCEP–DOE analysis datasets, (c) ERA-40, and (d) NCEP–DOE over the regions of 17°–23°N, 110°–120°E during May and June 1998. (e)–(h) As in (a)–(d), but for the Q_2 profiles. Units are K day^{-1}.

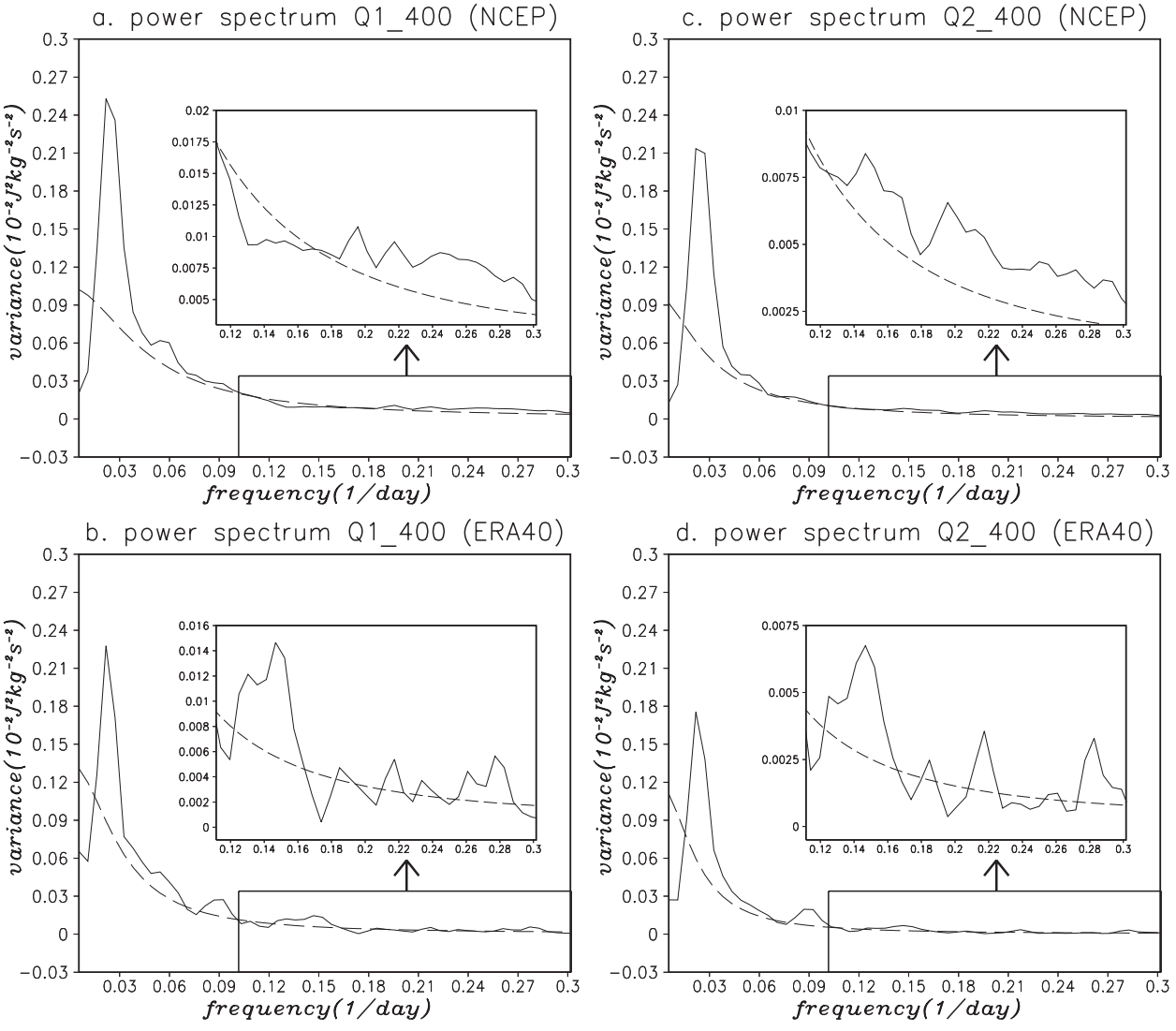

FIG. 2. Power spectra of 400-hPa apparent heat source (Q_1) during summer (July–September) over the WNP (0°–35°N, 110°–170°E) based on (a) NCEP–DOE and (b) ERA-40. (c),(d) As in (a),(b), but for Q_2. Dashed lines represent the red noise spectrum. The annual cycle is removed before computation of the spectrum analysis.

(Maloney and Hartmann 2001; Part I) or the changes of the background vertical shear associated with the ISO flow (Li 2006). It was found that the synoptic disturbances tend to grow faster (slower) under an easterly (westerly) vertical shear (Li 2006). Thus the low-level westerly coupled with the high-level easterly during an ISO active phase may set up a favorable environment for the development of the synoptic-scale disturbances over the WNP.

In the following, we examine how SSV feeds back to the intraseasonal apparent heat and moisture sources. This involves two steps of calculations. First, all the variables (e.g., u, v, ω, T, q) are partitioned into the LFBS, intraseasonal, and synoptic-scale components. Then we calculate the Q_1 and Q_2 fields based on the total components (i.e., the sum of the LFBS, intraseasonal, and synoptic components). The so-calculated Q_1 and Q_2 fields are then subjected to a 10–90-day bandpass filter to illustrate the geographic distribution of the overall strength of the intraseasonal Q_1 and Q_2 variabilities.

The standard deviation of 1000–100-hPa-averaged 10–90-day heating rate (Q_1/c_p) calculated based on the total fields above is displayed in Fig. 4a. Note that the great intraseasonal diabatic heating is evident over the strong mean convection regions. Three maximum variability centers are identified, and they are located in the Indian monsoon region (10°–20°N, 70°–100°E), the Philippine Sea–WNP sector (10°–20°N, 120°–150°E), and the tropical eastern Pacific (5°–15°N, 90°–120°W), as shown in

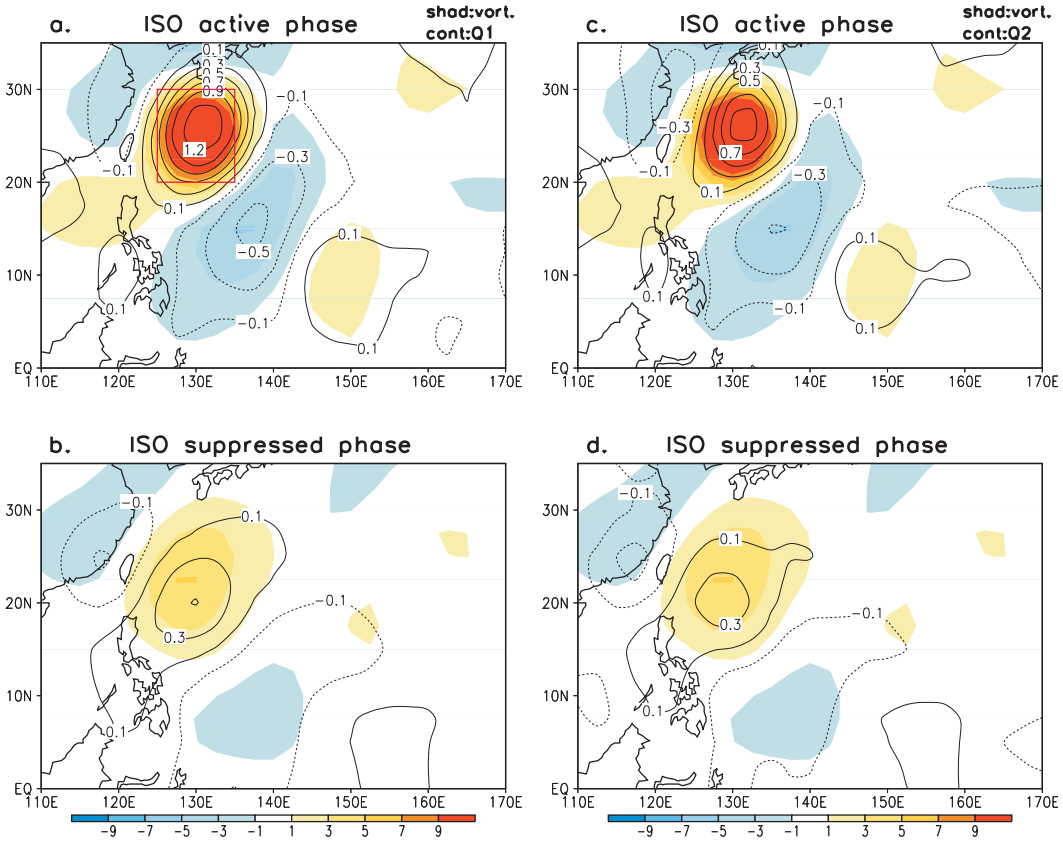

FIG. 3. Synoptic-scale (3–10 day) 850-hPa vorticity (shading, 10^{-6} s^{-1}) and vertically averaged (left) Q_1/c_p and (right) Q_2/c_p fields (contour, K day^{-1}) regressed based on the 3–10-day 850-hPa vorticity index at (20°–30°N, 125°–135°E) denoted by a red box during the ISO (top) active and (bottom) suppressed phases.

Fig. 4a. The spatial pattern of the 10–90-day diabatic heating corresponds well to the gross features of the intraseasonal precipitation as identified in Fu and Wang (2004), reflecting the diabatic heat source for the intraseasonal rainfall. The vertical profiles of the apparent heat sources averaged over the Indian Ocean and tropical western and eastern Pacific show a maximum value near 400–500 hPa, with a heating rate of 2–2.5 K day^{-1} (Fig. 4d).

In the second step, we assess the effects of synoptic eddies on the intraseasonal apparent heat source. Two methods are developed for this purpose. One is to calculate the Q_1 and Q_2 fields based on the sum of the LFBS and synoptic (LS) components of the individual fields without the involvement of ISO. Here we give the horizontal advection of temperature in the Q_1 as an example, which may be written as $c_p[(\overline{\overline{\mathbf{V}}} + \mathbf{V}') \cdot \nabla(\overline{\overline{T}} + T')]$. The so-calculated Q_1 and Q_2 fields are then subjected to a 10–90-day bandpass filter to illustrate how SSV nonlinearly rectifies the intraseasonal apparent heating fields through the eddy–LFBS interaction. This calculation, however, does not include the effect of the eddy–ISO interaction. The standard deviation of the vertically averaged, 10–90-day heating rate (Q_1/c_p) calculated based on the LS components is displayed in Fig. 4b. The amplitude of the nonlinearly rectified heating field over the tropical Indian Ocean and western Pacific regions is 0.2–0.25 K day^{-1} (Fig. 4b), and is much smaller than that of the total intraseasonal heating rate (Q_1/c_p) (Fig. 4a). The vertical profiles of the nonlinearly rectified heating fields averaged over the three active ISO regions show the maximum amplitude in the midtroposphere (Fig. 4e).

The second method has the following procedure: 1) calculating Q_1 and Q_2 with the sum of the LFBS and ISO (hereafter LI) components, 2) applying a 10–90-day bandpass filter to the resulting Q_1 and Q_2 fields, and 3) subtracting the time series of the intraseasonal Q_1 and Q_2 fields above from the time series of the intraseasonal Q_1 and Q_2 fields calculated based on the total components. The difference fields reflect the eddy interactions with both the LFBS and ISO components. The second method is called the T-LI method.

The amplitude of the nonlinearly rectified Q_1 field derived by the T-LI method is a little weaker (Fig. 4c), compared with that derived based on the LS components

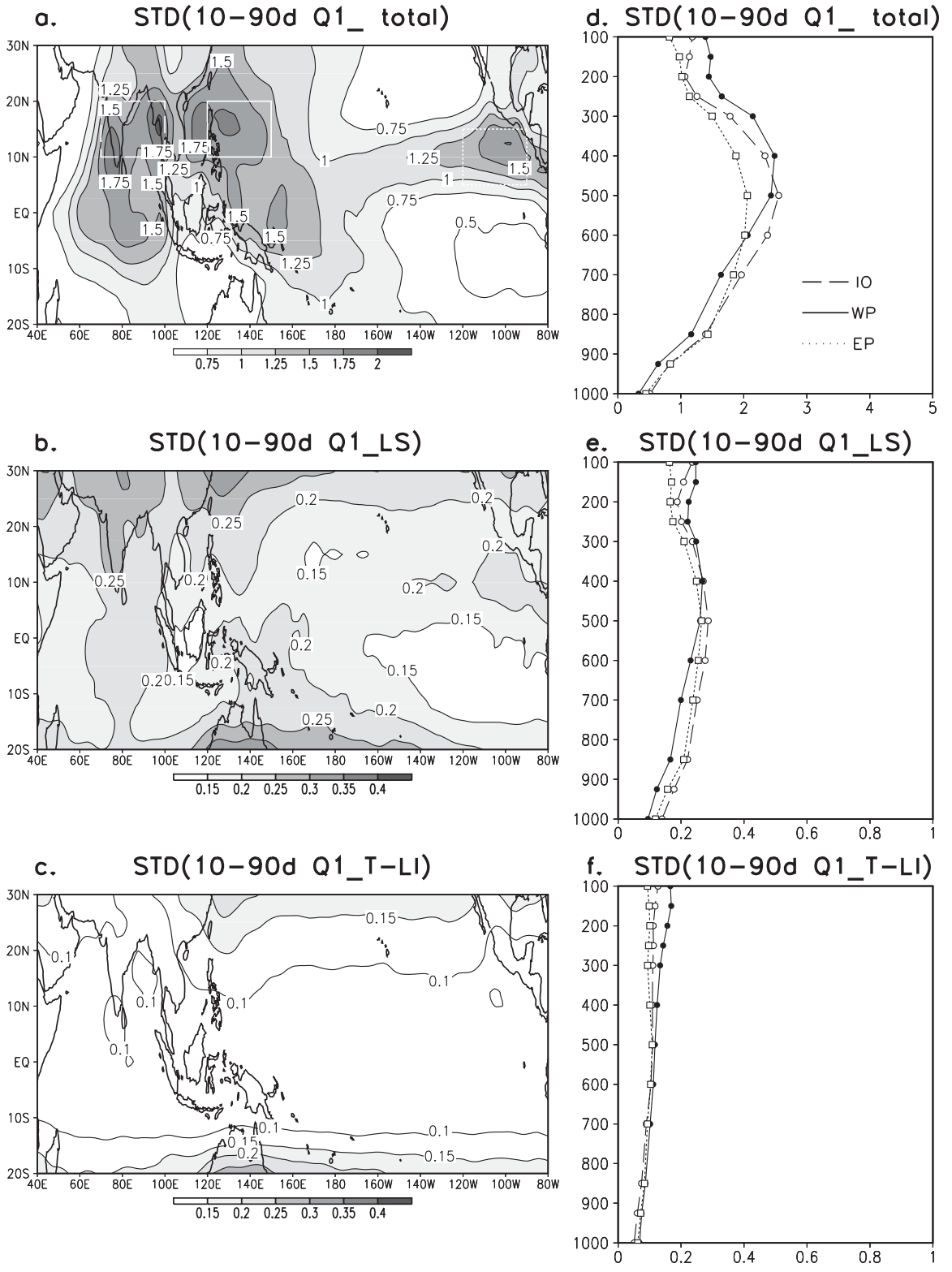

FIG. 4. Standard deviations of vertically averaged 10–90-day heating rates (Q_1/c_p, K day^{-1}) calculated based on the (a) total fields, (b) LS components, and (c) T-LI method. (d)–(f) Vertical profiles of (a)–(c) averaged over the Indian monsoon region [(10°–20°N, 70°–100°E); a long dashed box in (a)], the Philippine Sea–WNP sector [(10°–20°N, 120°–150°E); a solid box in (a)], and the tropical eastern Pacific [(5°–15°N, 90°–120°W); a short dashed box in (a)].

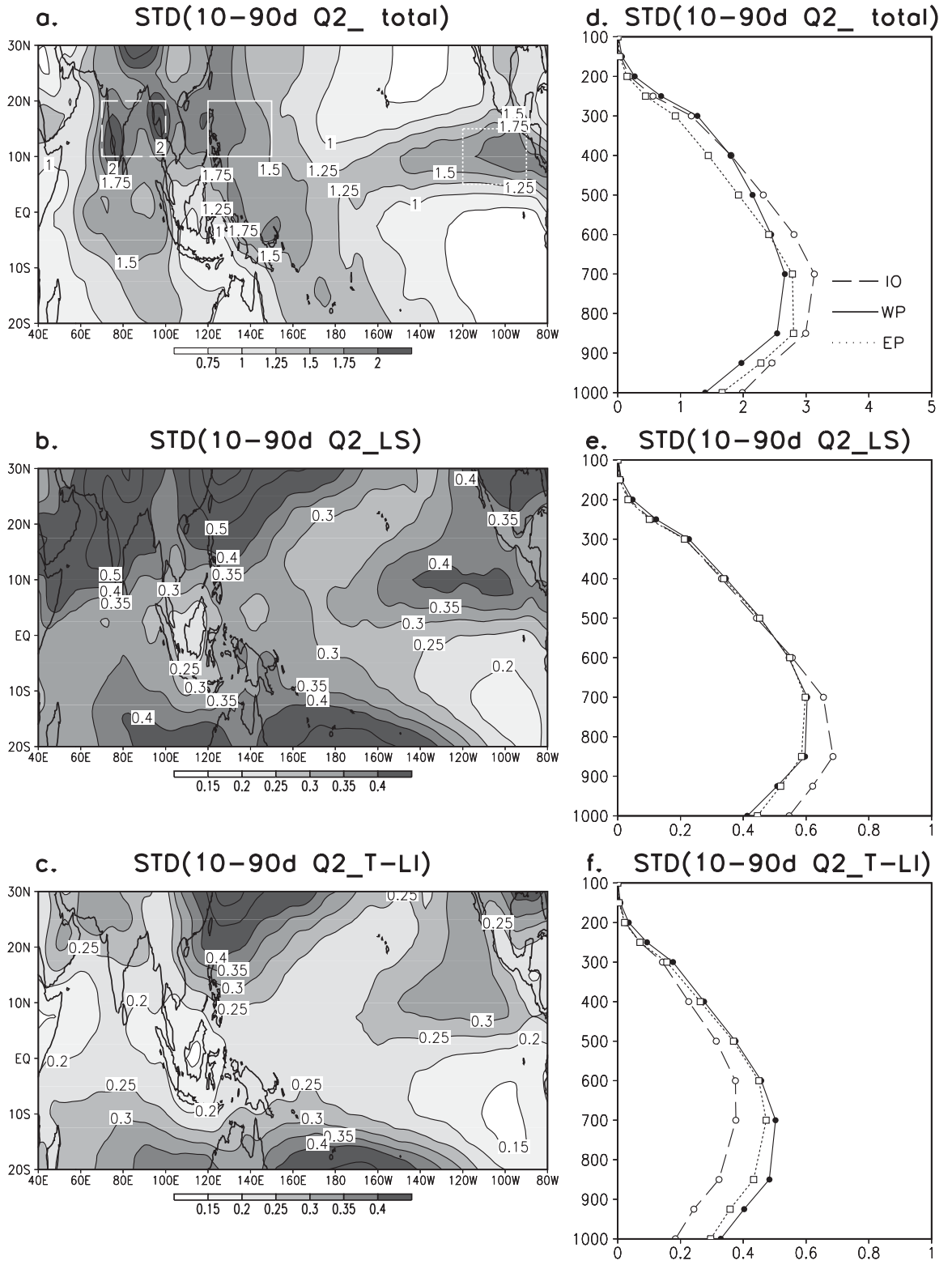

FIG. 5. As in Fig. 4, but for Q_2/c_p (K day^{-1}).

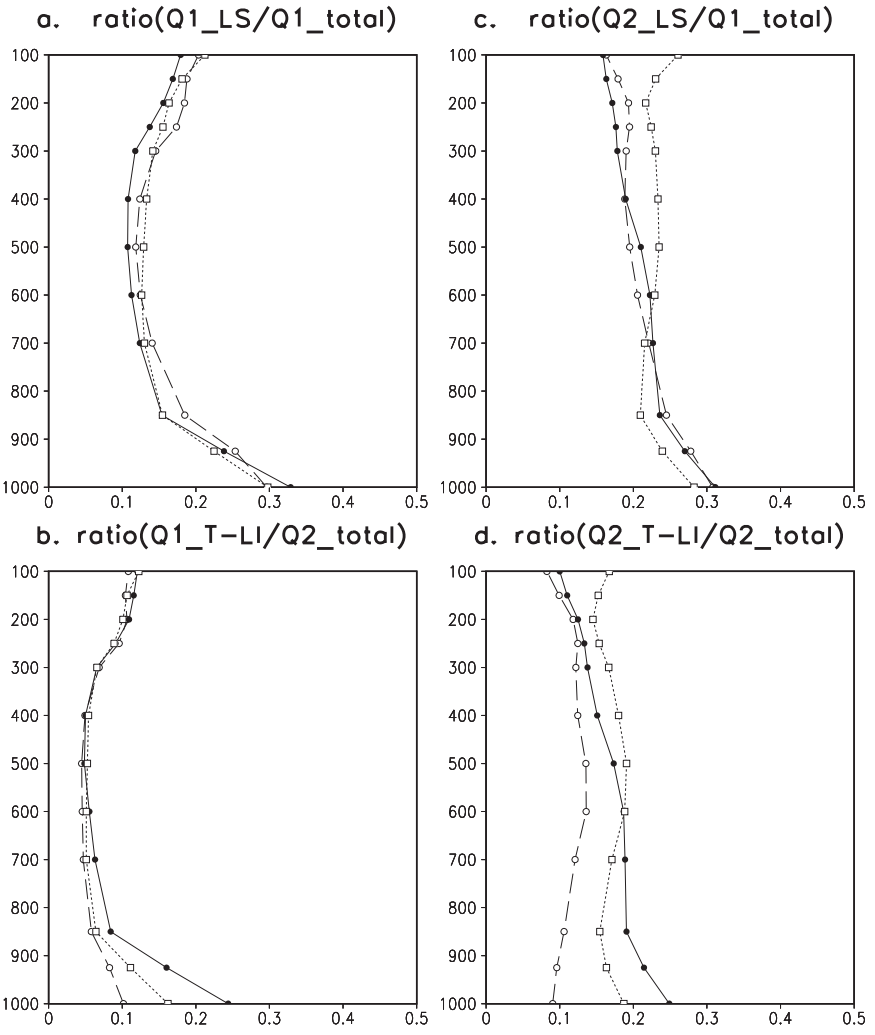

FIG. 6. Vertical distributions of the ratios of the standard deviations of the nonlinear rectified 10–90-day Q_1 field calculated based on the (a) LS components and (b) T-LI method vs the standard deviations of the total intraseasonal Q_1 over the three box regions shown in Fig. 4. (c),(d) As in (a),(b), but for Q_2.

(Fig. 4b), even though their spatial distributions are similar. The vertical profiles of the heating show a maximum rate on the order of 0.1–0.2 K day^{-1} in the upper troposphere (Fig. 4f). The results imply that the eddy–ISO interaction, which is excluded in the calculation based on the LS components, tends to weaken the nonlinear rectification of the apparent heating.

The same methods are applied to the Q_2 field. The overall horizontal patterns of the calculated intraseasonal Q_2 fields (Figs. 5a–c) are quite similar to the corresponding Q_1 fields (Figs. 4a–c). However, the vertical profiles of the Q_2 field are markedly different. The maximum amplitudes of the total and nonlinearly rectified intraseasonal Q_2 fields all appear in the lower troposphere (between 700 and 850 hPa). Comparing the vertical profiles in Fig. 5 with those in Fig. 4, one can find that while the total intraseasonal Q_1 and Q_2 have the same magnitude, the nonlinearly rectified Q_2 has larger amplitudes than the Q_1. This might be attributed to the nonlinearly rectified radiative cooling effect that somehow opposes the rectified convective heating effect. A further diagnostic study is needed to reveal their relationship. The results above suggest that the synoptic-scale perturbation, through its interaction with the mean flow, may significantly modulate the ISO heating.

To quantitatively determine the SSV-to-ISO upscale feedback, we calculate the ratios of the standard deviations of the nonlinearly rectified Q_1 and Q_2 derived based on the aforementioned two methods versus the standard deviation of the total intraseasonal Q_1 and Q_2 fields. It turns out that the nonlinearly rectified Q_1 and Q_2 based on the LS components account for 12%–30%

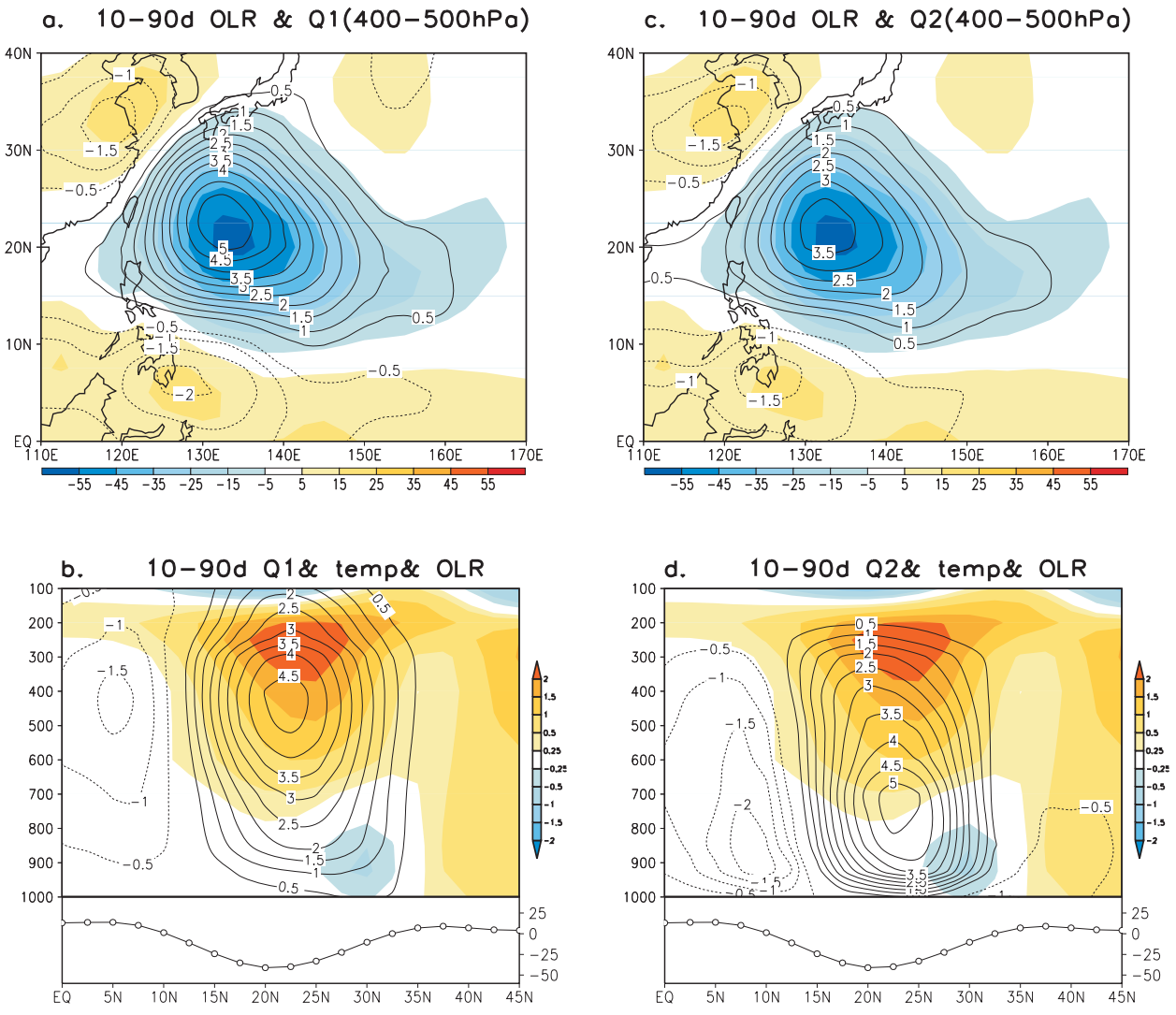

FIG. 7. ISO active minus suppressed composites of (a) spatial phase relationships between the 10–90-day OLR (shading, W m^{-2}) and 400–500-hPa averaged Q_1/c_p based on the total fields (contour, K day^{-1}) and (b) latitude–vertical sections of the 10–90-day temperature (shading; K) and Q_1/c_p (contour, K day^{-1}) fields, along with the meridional profile of OLR (W m^{-2}) averaged at 130°–140°E. (c),(d) As in (a),(b), but for Q_2/c_p (K day^{-1}).

of the total intraseasonal Q_1 and Q_2 variabilities in the three active ISO regions (Figs. 6a,c). The ratios calculated based on the T-LI method drop over all the regions. The largest drop appears in the Indian monsoon region, while the ratios over the tropical western Pacific (the region of focus in this study) drop slightly and remain at 10%–25% (Figs. 6b,d). The maximum ratios often appear near the surface (Fig. 6).

To reveal the spatial phase relationship between the ISO convection and the apparent heating, we show the active minus suppressed composite of the total intraseasonal Q_1 and Q_2 fields, OLR, and temperature fields. The intraseasonal Q_1 and Q_2 fields are in general in phase with the ISO convection, with the maximum heating centers located slightly to the northwest of the negative OLR center (Figs. 7a,c). The vertical profiles of the apparent heating and temperature fields averaged along 130°–140°E (where the ISO convection center is located) are shown in Figs. 7b,d. Both the vertical structures of Q_1 and Q_2 show the same signs throughout the troposphere. The maximum heating centers associated with Q_1 and Q_2 occur in the mid- and lower troposphere, respectively (Figs. 7b,d). A positive temperature anomaly appears slightly north of the ISO convection center and is collocated with the apparent heating centers. The positive temperature anomaly has a maximum center in the upper troposphere (around 200–300 hPa). The spatial phase relationships shown in Fig. 7 suggest that the apparent

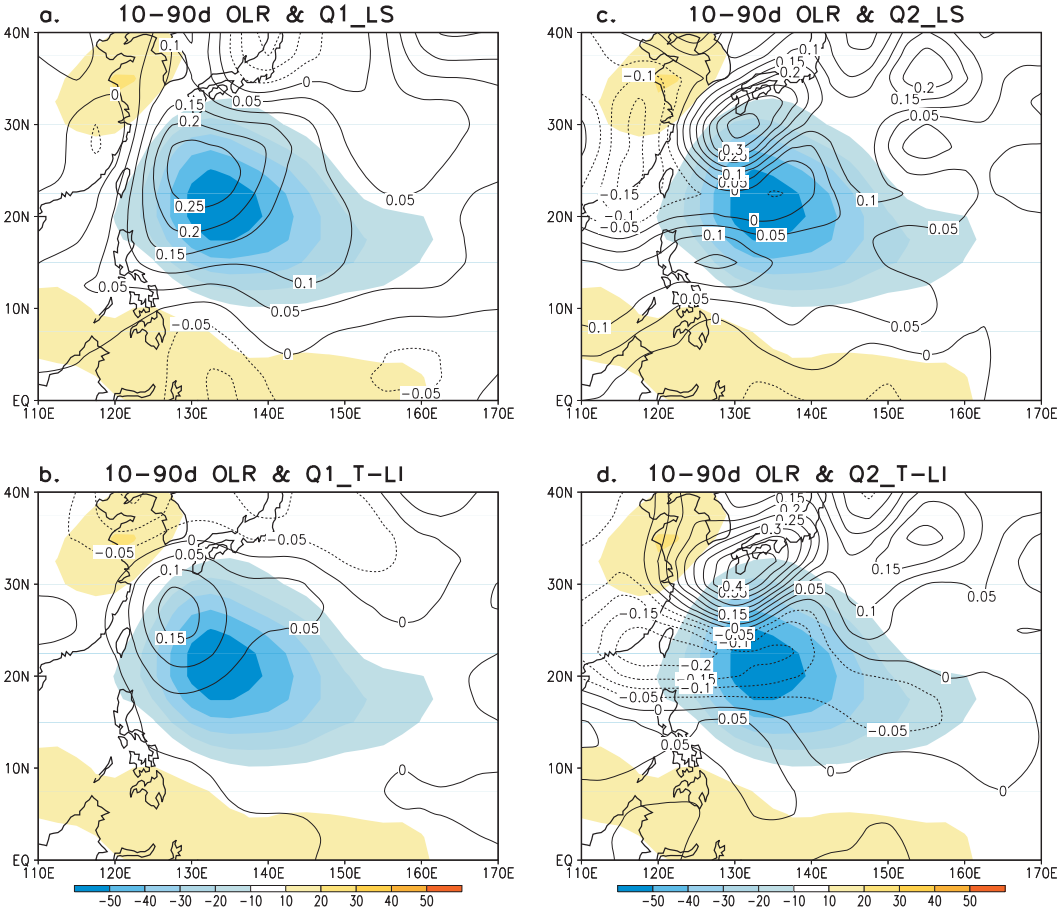

FIG. 8. As in Figs. 7a,c, except for the nonlinearly rectified 10–90-day Q_1/c_p and Q_2/c_p fields calculated based on the (a),(c) LS components and (b),(d) T-LI method.

heating fields may play a role in the northwestward propagation of the ISO convection in the WNP.

The intraseasonal heating fields in Fig. 7 include the contributions from the ISO and other scale motions. To determine whether the synoptic-scale disturbances contribute to the northwestward shift of the intraseasonal heating, we examine the phase relationship between the ISO convection and the nonlinear rectified 10–90-day Q_1 and Q_2 heating fields calculated based on the LS components and the T-LI method, respectively (Fig. 8). The nonlinear rectified intraseasonal Q_1 and Q_2 fields based on the two methods show a marked northwestward shift relative to the ISO convective center. Thus the observational analysis result suggests that the eddy–mean flow interaction leads to the northwestward displacement of the intraseasonal atmospheric heating, which may further contribute to the northwestward movement of the ISO convection.

Figure 9 shows the vertical structures of the nonlinearly rectified Q_1 and Q_2 fields. A positive Q_1 heating center appears at 400–500 hPa (Figs. 9a,b). This heating partially contributes to the positive temperature perturbation near the ISO convection center. The diagnosis of each term in the apparent heat source budget equation [Eq. (1)] shows that both the horizontal temperature advection, $c_p(\mathbf{V} \cdot \nabla T)$, and adiabatic heating/cooling processes, $-c_p\omega\sigma$, are major terms that balance the Q_1 field.

The vertical profile of the 10–90-day Q_2 field induced by the nonlinear rectification of synoptic disturbances is featured by a baroclinic vertical structure near the ISO convection center. The positive heating in the upper level is coupled with a cooling in the lower level (Figs. 9c,d). Our diagnosis shows that the vertical advection term $[-L\omega(\partial q/\partial p)]$ primarily contributes to this baroclinic structure of Q_2 (figure not shown). Compared to the total intraseasonal heating shown in Fig. 7, the magnitude of the nonlinear rectified intraseasonal Q_2 (Figs. 8, 9) is only about one-tenth of that. Thus the SSV-induced nonlinear rectification will not change the sign of the intraseasonal heating.

In summary, the synoptic-scale (3–10 day) apparent heat and moisture sources are well collocated with the

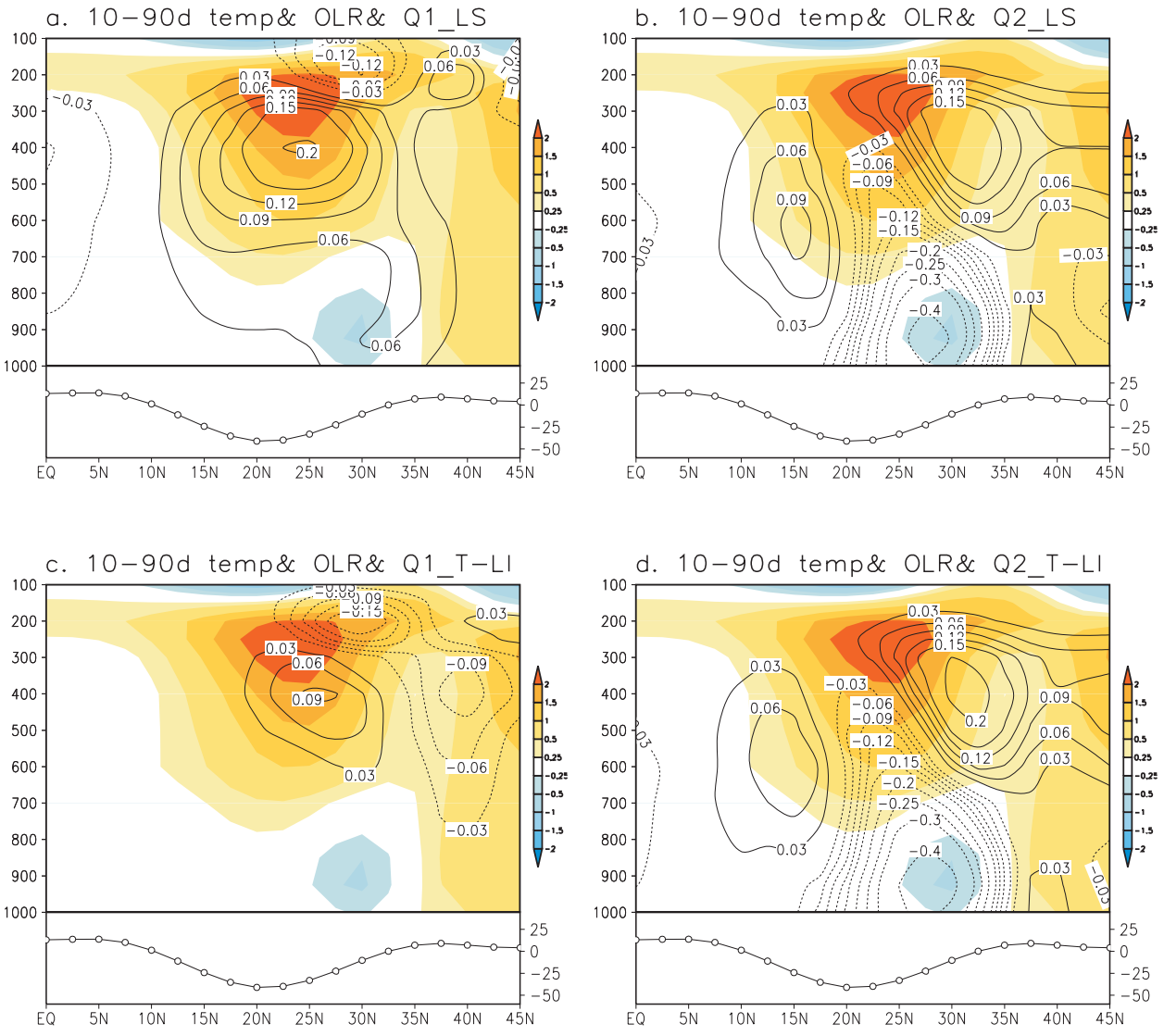

FIG. 9. As in Figs. 7b,d, except for the nonlinearly rectified 10–90-day Q_1/c_p and Q_2/c_p fields calculated based on the (a),(b) LS components and (c),(d) T-LI method.

synoptic-scale vorticity field, and both are greatly modulated by the boreal summer ISO over the WNP. SSV, on the other hand, exerts an upscale feedback to the ISO by modulating the distribution of the intraseasonal apparent heating. The nonlinearly rectified intraseasonal Q_1 and Q_2 fields have a maximum center to the northwest of the ISO convection center and thus may contribute to the northwestward propagation of ISO in the WNP.

4. Impact of eddy momentum transport on the ISO wind

In this section, through the analysis of the effect of synoptic eddy momentum transports on the ISO zonal wind, we investigate another type of atmospheric upscale feedback process. First we partition each atmospheric variable in the zonal momentum equation into synoptic-scale (3–10 day) and low-frequency (with periods longer than 10 days) components. Applying a 10-day low-pass filter operator, the mean zonal momentum equation may be written as

$$\frac{\partial \overline{u}}{\partial t} = -\overline{\frac{\partial u'u'}{\partial x}} - \overline{\frac{\partial u'v'}{\partial y}} - \overline{\frac{\partial u'\omega'}{\partial p}} - \overline{u}\,\overline{\frac{\partial u}{\partial x}} - \overline{v}\,\overline{\frac{\partial u}{\partial y}} - \overline{\omega}\,\overline{\frac{\partial u}{\partial p}} - \overline{\frac{\partial \phi}{\partial x}} + f\overline{v}, \tag{3}$$

where t denotes time, u and v denote zonal and meridional wind fields, respectively, ω is vertical p velocity,

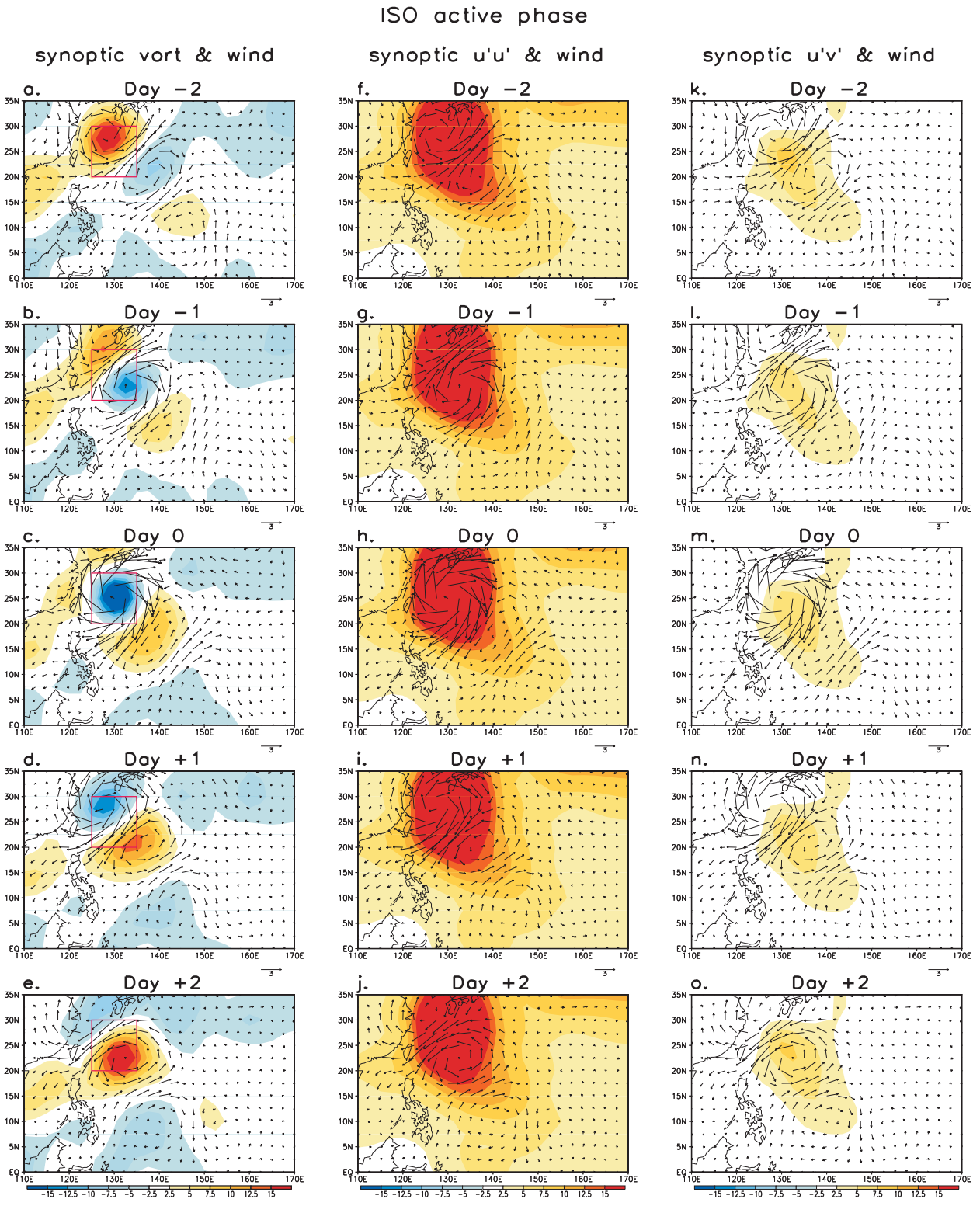

FIG. 10. (a)–(e) Synoptic-scale (3–10 day) vorticity (shading; 10^{-6} s^{-1}) and wind (vector, m s^{-1}) fields at 850 hPa regressed based on the time series of 3–10-day vorticity at (20°–30°N, 125°–135°E) denoted by a red box from day −2 to day +2 day during the ISO active phase. (f)–(j),(k)–(o) As in (a)–(e), but the shadings are for the zonal and meridional eddy momentum flux ($u'u'$, $u'v'$) fields (m^2 s^{-2}), respectively.

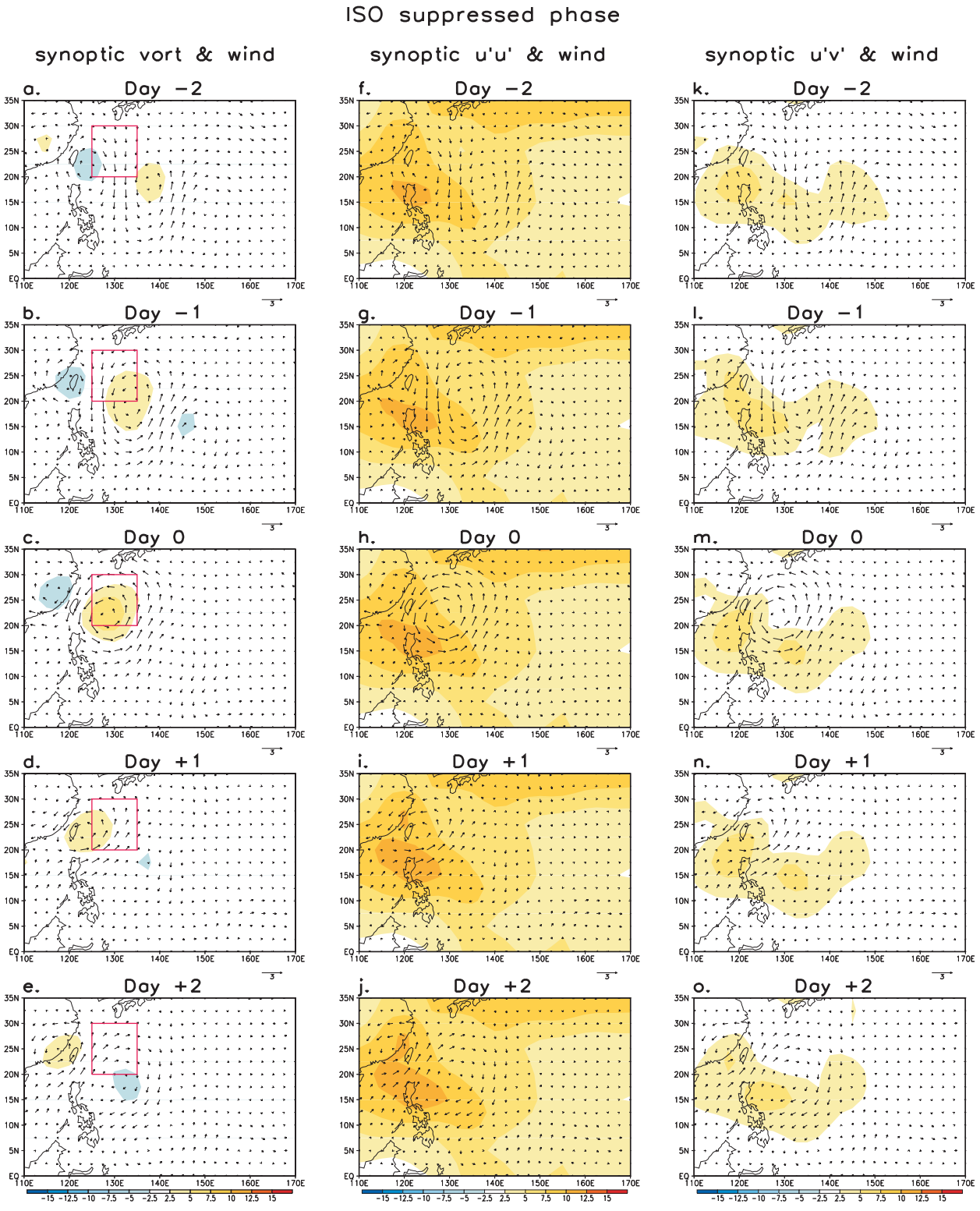

FIG. 11. As in Fig. 10, but for the ISO suppressed phase.

p is pressure, ϕ is geopotential, and f is the Coriolis parameter. A prime represents the 3–10-day, synoptic-scale variable, and an overbar designates the low-pass (longer than 10 days) filter operator. The left-hand side of Eq. (3) consists of the zonal wind tendency on both the LFBS and ISO time scales. To derive the intraseasonal zonal wind tendency, we introduce a difference operator at both sides of Eq. (3). The difference operator $\Delta()$ is defined as $() - \overline{\overline{()}}$, where a double overbar denotes a 90-day low-pass filter operator (see section 3 of Part I for a detailed description of this strategy). Thus the intraseasonal zonal wind tendency may be written as

$$\frac{\partial \tilde{u}}{\partial t} = \underbrace{\Delta\left(-\frac{\overline{\partial u'u'}}{\partial x} - \frac{\overline{\partial u'v'}}{\partial y} - \frac{\overline{\partial u'\omega'}}{\partial p}\right)}_{\text{A}} + \underbrace{\Delta\left(-\overline{u}\frac{\overline{\partial u}}{\partial x} - \overline{v}\frac{\overline{\partial u}}{\partial y} - \overline{\omega}\frac{\overline{\partial u}}{\partial p}\right) + \Delta\left(-\frac{\overline{\partial \phi}}{\partial x}\right) + \Delta f\overline{v}}_{\text{B}} \tag{4}$$

where a tilde denotes the intraseasonal component. Equation (4) states that the ISO zonal wind tendency is determined by the eddy momentum flux convergence (term A) and ISO motion–related processes (term B) including advection, pressure gradient force, and Coriolis force. Before conducting an ISO zonal momentum budget, we first examine the synoptic eddy momentum transport terms.

The dominant synoptic-scale vorticity and eddy momentum flux patterns in the WNP during the ISO active and suppressed phases are displayed in Figs. 10 and 11, respectively. As the patterns derived from the NCEP–DOE and ERA-40 datasets show similar features, only the averaged results are shown. Based on the synoptic-scale (3–10 day) vorticity index at the WNP box (20°–30°N, 125°–135°E), we examine the evolution and structure of the synoptic vorticity, wind, and eddy momentum flux fields by performing a lagged regression analysis. During the ISO active phase, an alternating cyclonic and anticyclonic vorticity wave train, oriented in a northwest–southeast direction, is clearly presented over the WNP. This wave train pattern is 180° out of phase in space between day −2 and +1, indicating the near 6-day periodicity. The wave train reveals a northwestward-propagating track during its evolution (Figs. 10a,e). It is interesting to note that even though the synoptic disturbances continuously move northwestward, the maximum zonal and meridional eddy momentum fluxes ($u'u'$ and $u'v'$) are approximately stationary (Figs. 10f–j and 10k–o, respectively). The maximum eddy momentum fluxes are located along the wave train track, where the synoptic variability is strongest. Compared with the horizontal eddy momentum flux, the vertical component of the eddy momentum flux is much weaker.

The northwestward-propagating synoptic vorticity wave trains are also identified over the WNP during the ISO suppressed phase, but with a marked reduction in the amplitudes (Figs. 11a–e). Accompanied with the weak synoptic disturbances, the eddy momentum flux terms during the ISO suppressed phase are about one-half of those during the ISO active phase. The maximum belts of $u'u'$ and $u'v'$ shift farther to the south and west, consistent with the southwestward displacement of the wave train track. They become more zonally elongated around 10°–20°N during the ISO suppressed phase (Figs. 11f–o).

The comparison of the results in Figs. 10 and 11 indicates that the amplitudes and distributions of the synoptic eddy momentum fluxes depend on the ISO phase. The ISO phase-dependent eddy momentum fluxes, on the other hand, may exert an upscale feedback to the ISO zonal wind, according to Eq. (4). Figure 12 shows the phase relationships between the eddy momentum flux convergence and the ISO zonal wind fields during the ISO active and suppressed phases, respectively. Here a green cross denotes the ISO cyclonic or anticyclonic vorticity center. It is found that the positive (negative) $\Delta[-(\partial\overline{u'u'}/\partial x)]$ and $\Delta[-(\partial\overline{u'v'}/\partial y)]$ occur at the transitional zone of the ISO zonal wind (where $\tilde{u} = 0$) during the ISO active (suppressed) phase. As a result, the synoptic eddy momentum transport tends to force a westerly (easterly) tendency to the north of the ISO westerly (easterly) center during the ISO active (suppressed) phase, promoting a northward propagation for ISO.

In addition to a northward propagation component, the eddy momentum transport also supports an eastward propagation component. However, this eastward propagation tendency is offset by other dynamical and physical processes, such as the westward shift of vorticity tendency due to the beta effect (Hsu and Weng 2001) and westward shift of surface humidity due to local air–sea interaction (Kemball-Cook and Wang 2001; Fu et al. 2003) and nonlinear rectification of the surface latent heat flux (Zhou and Li 2010), which favor the westward propagation. The final propagation direction depends on the net effect of the different processes. Obviously, the northwestward-forcing factors are greater. Therefore, we will focus below on the role of the eddy momentum transport in the northward propagation.

A detailed ISO zonal momentum budget is performed according to Eq. (4). Figure 13 illustrates the latitudinal

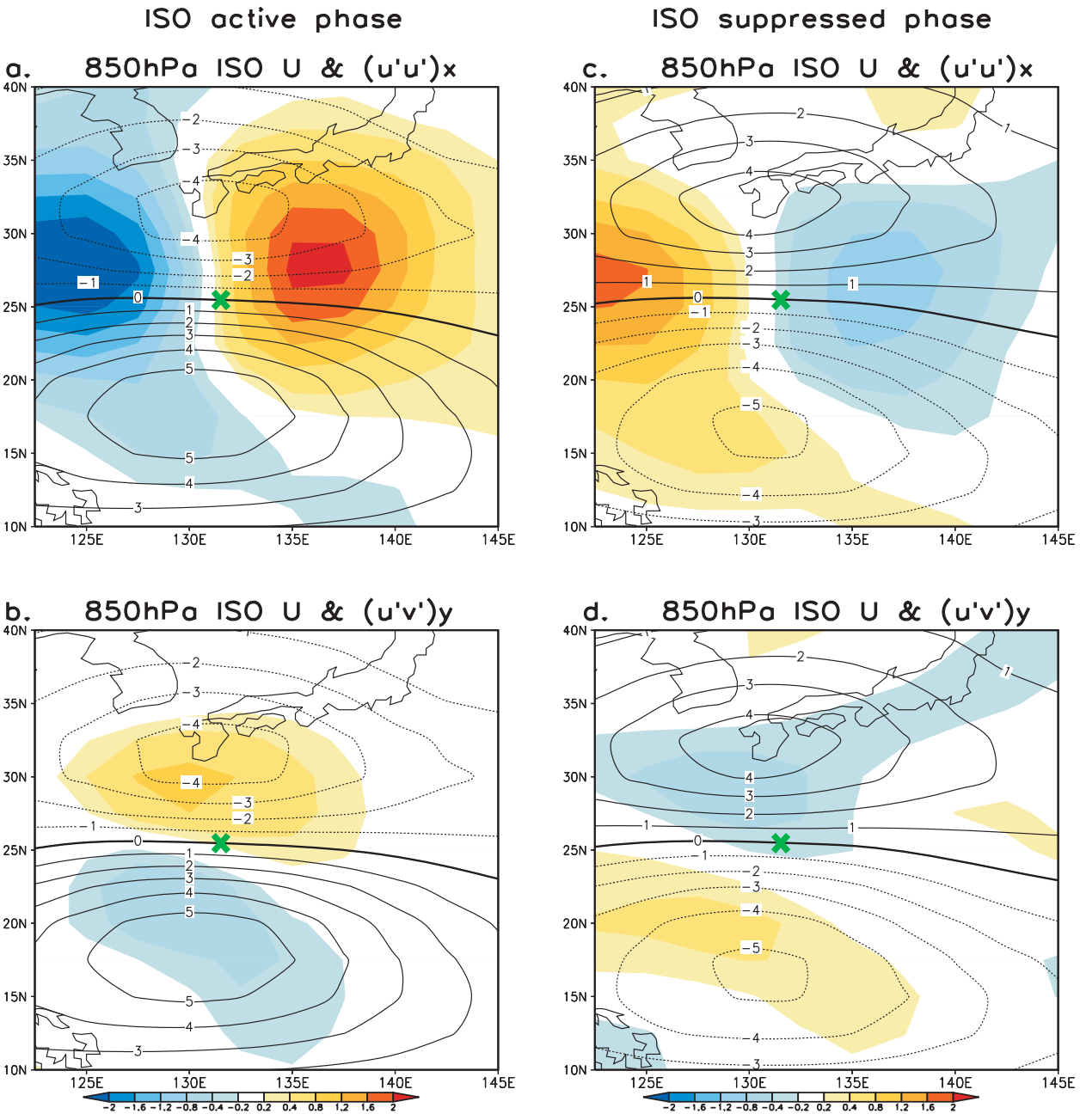

FIG. 12. (a) ISO active phase composites of the intraseasonal zonal wind (contour; m s^{-1}) and zonal eddy momentum flux convergence $[\Delta[-(\partial\overline{u'u'}/\partial x)]$; shading, 10^{-5} m $s^{-2}]$ at 850 hPa. A cross represents the ISO cyclonic center. (b) As in (a), but for the meridional eddy momentum flux convergence $[\Delta[-(\partial\overline{u'v'}/\partial y)]$; shading, 10^{-5} m $s^{-2}]$. (c),(d) As in (a),(b), but for the ISO suppressed phase composites.

distributions of key budget terms averaged along 130°–135°E where the maximum 850-hPa ISO zonal wind is located. The sum of all budget terms at the right-hand side of Eq. (4) is close to the observed tendency. They both show the westerly tendency in the transitional region of the ISO zonal wind. About 40% of the total tendency is attributed to the eddy momentum flux convergence (Fig. 13, top panel). Figure 13 (bottom panel) further presents the amplitude of each term at the transitional zone ($\tilde{u} = 0$).While the largest terms are the pressure gradient force and the Coriolis force, they are largely offset with each other. The advection terms

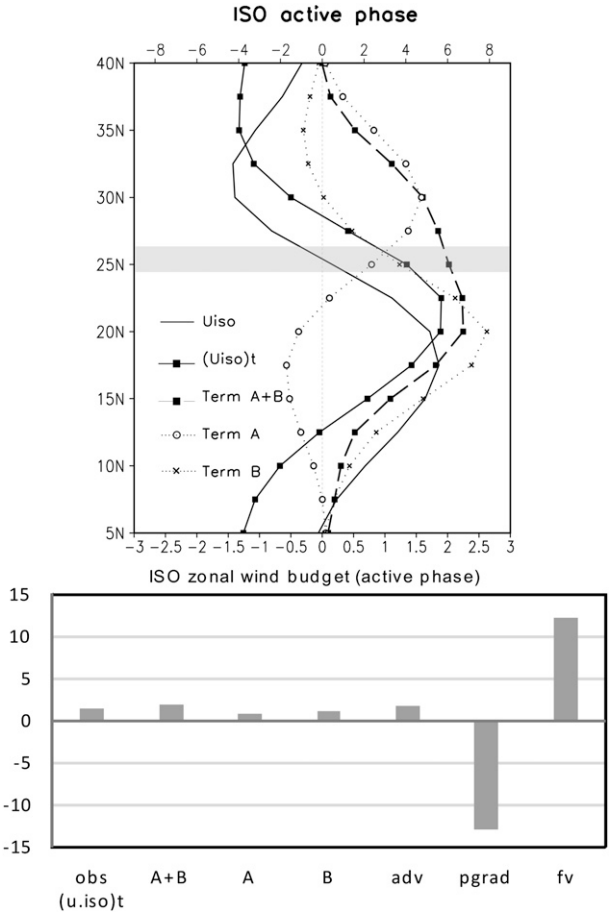

FIG. 13. (top) Latitudinal distributions along 130°–135°E of the ISO zonal wind at 850 hPa (solid black line; unit: m s^{-1} at top x-axis labels), the observed ISO zonal wind tendency (solid black line with squares), the sum of all budget terms on the rhs of Eq. (4) (dashed black line with squares), term A (dotted line with circles), and term B (dotted line with crosses) in Eq. (4) for the ISO active phase composite. The units for all tendency terms are 10^{-5} m s^{-2} at bottom x-axis labels. The gray shading zone indicates the transitional zone of the ISO zonal flow ($\tilde{u} = 0$). (bottom) Each of the budget terms in Eq. (4) (from left to right: observed ISO zonal wind tendency, the sum of terms A and B, term A, term B, advection, pressure gradient force, and Coriolis force) averaged at the transitional region (25°N, 130°–135°E) during the ISO active phase. Units: 10^{-5} m s^{-2}.

primarily contribute to a positive zonal wind tendency. The eddy momentum flux convergence (term A) and the net effect of ISO motion-related processes (term B) both account for the westerly tendency at the transitional region during the ISO active phase. A similar result is obtained during the ISO suppressed phase. The momentum budget analysis indicates that the eddy momentum transport may partially contribute to the northward propagation of ISO during both the active and suppressed phases.

The relative contributions of zonal, meridional, and vertical eddy momentum transports to the ISO zonal wind tendency are shown in Fig. 14. Along 130°–135°E, the horizontal eddy momentum transport terms are the main contributors to the ISO zonal wind tendency while the vertical component of the eddy momentum transport is small (Fig. 14). Both $\Delta(-\partial\overline{u'u'}/\partial x)$ and $\Delta(-\partial\overline{u'v'}/\partial y)$ generate a westerly (easterly) tendency at $\tilde{u} = 0$ during the ISO active (suppressed) phase. Thus, both the terms contribute to the northward propagation of the boreal summer ISO. Meanwhile, the eddy momentum transport terms tend to produce an easterly (westerly) tendency over the ISO westerly (easterly) center, thus acting to weaken the ISO flow.

Figure 15 further reveals the vertical distributions of three-dimensional eddy momentum transport fields at the transitional ($\tilde{u} = 0$) zone. The vertical component of the eddy momentum transport shows a negligible contribution to the ISO zonal wind tendency throughout the troposphere. During the ISO active (suppressed) phase, the zonal eddy momentum transport generates an intraseasonal westerly (easterly) tendency throughout the troposphere, whereas the meridional eddy momentum transport changes from a westerly (easterly) to easterly (westerly) tendency at 300 hPa (Fig. 15). The combined effect of the zonal and meridional transports leads to a westerly (easterly) tendency from the surface to 250 hPa during the ISO active (suppressed) phase.

5. Summary

The interactions between the boreal summer ISO and synoptic-scale disturbances over the WNP, with an emphasis on the upscale feedback from the higher- to lower-frequency variability, are investigated based on the diagnoses of the atmospheric apparent heat source (Q_1), apparent moisture sink (Q_2), and eddy momentum transport. An alternating 3–10-day heating and cooling pattern for Q_1 and Q_2 is in phase with a 3–10-day cyclonic and anticyclonic vorticity wave train, aligned in a northwest–southeast orientation. These synoptic heating/vorticity wave trains are vigorous and well organized during the ISO active phase, whereas they become dramatically weakened and loosely organized during the ISO suppressed phase. This indicates that the structure and intensity of the SSV depend on the ISO phases, and the ISO exerts a large-scale control over the generation and growth of synoptic disturbances, agreeing with previous studies (e.g., Maloney and Hartmann 2001; Straub and Kiladis 2003; Zhou and Li 2010; Part I).

The ISO phase-dependent synoptic fluctuations, on the other hand, exert an upscale feedback to the ISO through

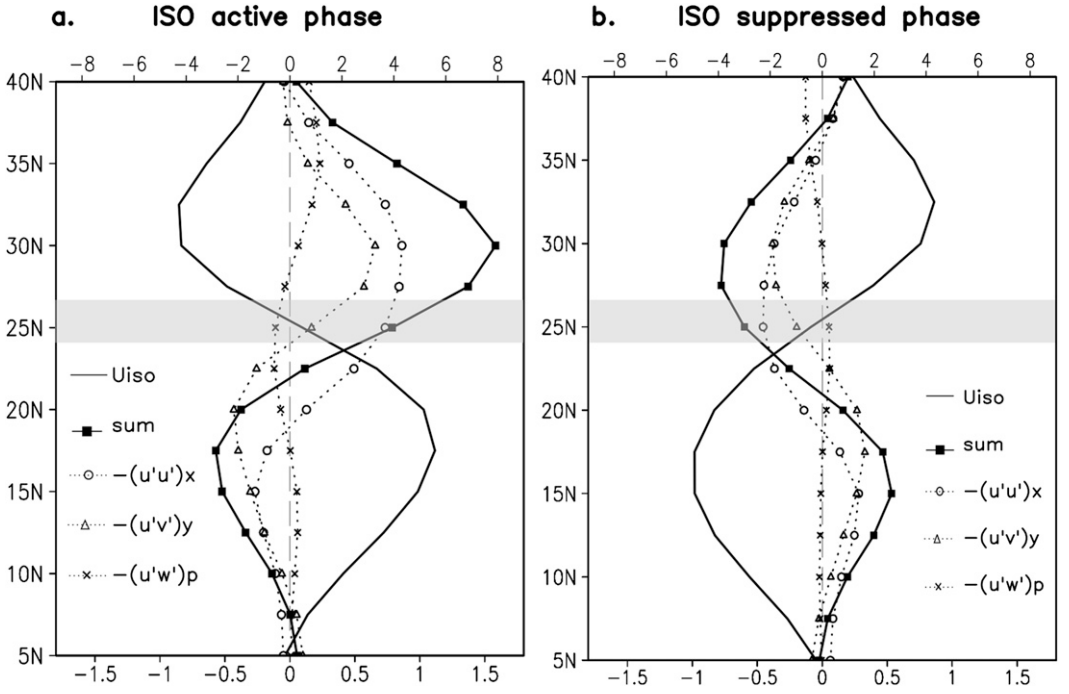

FIG. 14. (a) Latitudinal distributions along 130°–135°E of the ISO zonal wind at 850 hPa (black line; unit: m s^{-1} at top x-axis labels) and eddy momentum flux convergence terms (dotted line with circles: $\Delta[-(\partial\overline{u'u'}/\partial x)]$; dotted line with triangles: $\Delta[-(\partial\overline{u'v'}/\partial y)]$; dotted line with crosses: $\Delta[-(\partial\overline{u'\omega'}/\partial p)]$; solid black line with squares: the sum of the three terms; units: 10^{-5} m s^{-2} at bottom x-axis labels) for the ISO active phase composite. The gray shading zone indicates the transitional zone of the ISO zonal flow ($\bar{u} = 0$). (b) As in (a), but for the ISO suppressed phase composite.

the modulation of the apparent heat and moisture sources. The nonlinearly rectified apparent heat and moisture sources due to the synoptic eddy–mean flow interaction account for 10%–30% of the total intraseasonal Q_1 and Q_2 variabilities. Over the WNP, the nonlinearly rectified Q_1 and Q_2 fields are located to the northwest of the ISO convection center. Such a phase shift may contribute to the northwestward propagation of the ISO

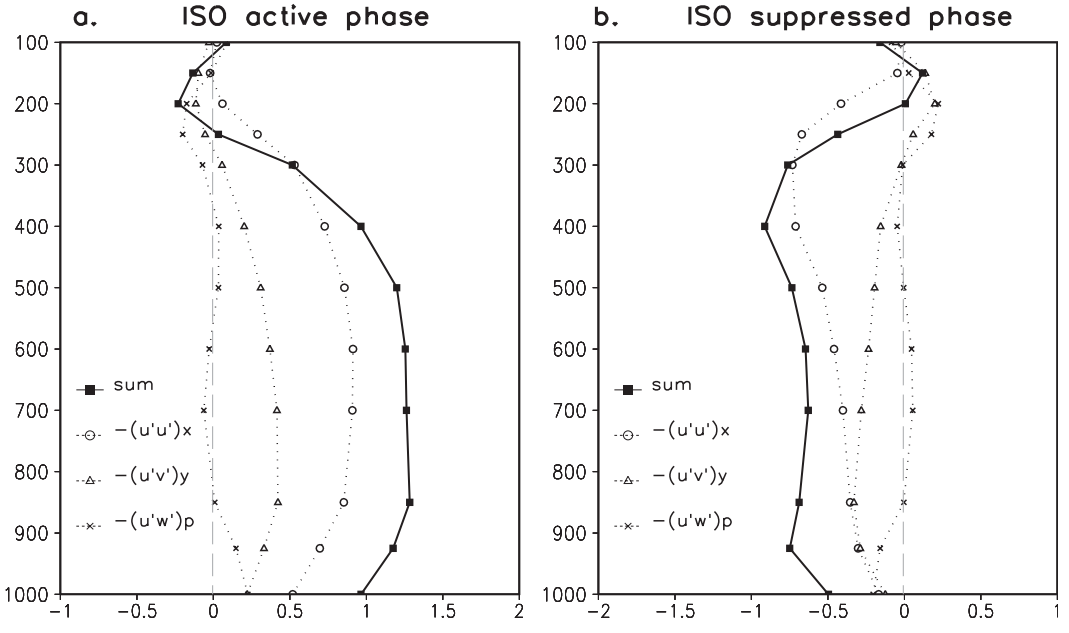

FIG. 15. As in Fig. 14, but for the vertical distributions of the eddy momentum flux convergence terms 10^{-5} m s^{-2} averaged along the ISO transitional zone.

over the WNP. The results above suggest an internal atmospheric dynamics mechanism through which an upscale feedback from SSV to ISO may take place. This result is complementary with the study by Zhou and Li (2010), which argued that SSV may modulate the ISO through the nonlinear rectification of the surface latent heat flux.

An additional upscale feedback process is through the eddy momentum transport. Although the synoptic-scale wave train continues to move northwestward in the WNP, the horizontal eddy momentum flux seems stationary and attains a maximum value along the wave train track. The accumulated synoptic momentum flux effect promotes a westerly (easterly) tendency in the ISO transitional zone ($\tilde{u} = 0$) during the ISO active (suppressed) phase, which favors the northward propagation of the ISO. Meanwhile, the eddy momentum transports tend to generate an easterly (westerly) tendency in the region of the ISO westerly (easterly), thus acting to decelerate the ISO flow. The diagnostic study provides observational evidence that supports the notion that there exists a two-way interaction between SSV and ISO, which has been a basis for various theoretical models (e.g., Biello and Majda 2005; Biello et al. 2007; Majda and Stechmann 2009).

The findings in Part II are complementary to the conclusions in Part I, which are based on the energetics diagnosis. Part II reveals more observational evidence of the synoptic contributions to the ISO propagation. While the major focus of the current study is on the scale interactions in the WNP, similar analyses may be conducted for other ISO active regions such as the tropical Indian Ocean and the tropical eastern Pacific.

Acknowledgments. Comments from two anonymous reviewers are greatly appreciated. This work was supported by NSC97-2917-I-564-154, NSC-097-2811-M-003-015, ONR Grants N000140810256 and N000141010774, and by the International Pacific Research Center that is sponsored by the Japan Agency for Marine-Earth Science and Technology (JAMSTEC), NASA (NNX07AG53G), and NOAA (NA17RJ1230).

REFERENCES

Biello, J. A., and A. J. Majda, 2005: A new multiscale model for the Madden–Julian oscillation. *J. Atmos. Sci.,* **62,** 1694–1721.

——, ——, and M. W. Moncrieff, 2007: Meridional momentum flux and superrotation in the multiscale IPESD MJO model. *J. Atmos. Sci.,* **64,** 1636–1651.

Chang, C.-P., J.-M. Chen, P. A. Harr, and L. E. Carr, 1996: Northwestward-propagating wave patterns over the tropical western North Pacific during summer. *Mon. Wea. Rev.,* **124,** 2245–2266.

Fu, X., and B. Wang, 2004: Differences of boreal summer intraseasonal oscillations simulated in an atmosphere–ocean coupled model and an atmosphere-only model. *J. Climate,* **17,** 1263–1271.

——, ——, T. Li, and J. McCreary, 2003: Coupling between northward-propagating, intraseasonal oscillations and sea surface temperature in the Indian Ocean. *J. Atmos. Sci.,* **60,** 1733–1753.

Hamming, R. W., 1989: *Digital Filters*. Prentice-Hall, 284 pp.

Hodges, K. I., B. J. Hoskins, J. Boyle, and C. Thorncroft, 2003: A comparison of recent reanalysis datasets using objective feature tracking: Storm tracks and tropical easterly waves. *Mon. Wea. Rev.,* **131,** 2012–2037.

Hsu, H.-H., and C.-H. Weng, 2001: Northwestward propagation of the intraseasonal oscillation in the western North Pacific during the boreal summer: Structure and mechanism. *J. Climate,* **14,** 3834–3850.

Hsu, P.-C., T. Li, and C.-H. Tsou, 2011: Interactions between boreal summer intraseasonal oscillations and synoptic-scale disturbances over the western North Pacific. Part I: Energetics diagnosis. *J. Climate,* **24,** 940–959.

Jiang, X., T. Li, and B. Wang, 2004: Structures and mechanisms of the northward propagating boreal summer intraseasonal oscillation. *J. Climate,* **17,** 1022–1039.

Johnson, R. H., and P. E. Ciesielski, 2002: Characteristics of the 1998 summer monsoon onset over the northern South China Sea. *J. Meteor. Soc. Japan,* **80,** 561–578.

Kanamitsu, M., W. Ebisuzaki, J. Woollen, S.-K. Yang, J. J. Hnilo, M. Fiorino, and G. L. Potter, 2002: NCEP–DOE AMIP-II reanalysis (R-2). *Bull. Amer. Meteor. Soc.,* **83,** 1631–1643.

Kawamura, R., T. Murakami, and B. Wang, 1996: Tropical and midlatitude 45-day perturbations over the western Pacific during the northern summer. *J. Meteor. Soc. Japan,* **74,** 867–890.

Kemball-Cook, S. R., and B. Wang, 2001: Equatorial waves and air–sea interaction in the boreal summer intraseasonal oscillation. *J. Climate,* **14,** 2923–2942.

Lau, K.-H., and N.-C. Lau, 1990: Observed structure and propagation characteristics of tropical summertime synoptic-scale disturbances. *Mon. Wea. Rev.,* **118,** 1888–1913.

Li, T., 2006: Origin of the summertime synoptic-scale wave train in the western North Pacific. *J. Atmos. Sci.,* **63,** 1093–1102.

Liebmann, B., and C. A. Smith, 1996: Description of a complete (interpolated) outgoing longwave radiation dataset. *Bull. Amer. Meteor. Soc.,* **77,** 1275–1277.

Madden, R. A., and P. R. Julian, 1971: Detection of a 40-50 day oscillation in the zonal wind in the tropical Pacific. *J. Atmos. Sci.,* **28,** 702–708.

Majda, A. J., and S. N. Stechmann, 2009: A simple dynamical model with features of convective momentum transport. *J. Atmos. Sci.,* **66,** 373–392.

Maloney, E. D., 2009: The moist static energy budget of a composite tropical intraseasonal oscillation in a climate model. *J. Climate,* **22,** 711–729.

——, and D. L. Hartmann, 2001: The Madden–Julian oscillation, barotropic dynamics, and North Pacific tropical cyclone formation. Part I: Observations. *J. Atmos. Sci.,* **58,** 2545–2558.

——, and M. J. Dickinson, 2003: The intraseasonal oscillation and the energetics of summertime tropical western North Pacific synoptic-scale disturbances. *J. Atmos. Sci.,* **60,** 2153–2168.

Marques, C. A. F., A. Rocha, and J. Corte-Real, 2010: Comparative energetics of ERA-40, JRA-25 and NCEP-R2 reanalysis, in the wave number domain. *Dyn. Atmos. Oceans,* **50,** 375–399.

Matthews, A. J., and G. N. Kiladis, 1999: The tropical–extratropical interaction between high-frequency transients and the Madden–Julian oscillation. *Mon. Wea. Rev.,* **127,** 661–677.

Straub, K. H., and G. N. Kiladis, 2003: Interactions between the boreal summer intraseasonal oscillation and higher-frequency tropical wave activity. *Mon. Wea. Rev.,* **131,** 781–796.

Tam, C. Y., and T. Li, 2006: The origin and dispersion characteristics of the observed tropical summertime synoptic-scale waves over the western Pacific. *Mon. Wea. Rev.,* **134,** 1630–1646.

Tsou, C.-H., P.-C. Hsu, W.-S. Kau, and H.-H. Hsu, 2005: Northward and northwestward propagation of 30-60 day oscillation in the tropical and extra-tropical western North Pacific. *J. Meteor. Soc. Japan,* **83,** 711–726.

Uppala, S. M., and Coauthors, 2005: The ERA-40 Re-Analysis. *Quart. J. Roy. Meteor. Soc.,* **131,** 2961–3012.

Wang, B., and H. Rui, 1990: Dynamics of the coupled moist Kelvin-Rossby wave on an equatorial β plane. *J. Atmos. Sci.,* **47,** 397–413.

——, and X. Xie, 1997: A model for the boreal summer intraseasonal oscillation. *J. Atmos. Sci.,* **54,** 72–86.

Xie, P., and P. A. Arkin, 1997: Global precipitation: A 17-year monthly analysis based on gauge observations, satellite estimates, and numerical model outputs. *Bull. Amer. Meteor. Soc.,* **78,** 2539–2558.

Yanai, M., S. Esbensen, and J.-H. Chu, 1973: Determination of bulk properties of tropical cloud clusters from large-scale heat and moisture budgets. *J. Atmos. Sci.,* **30,** 611–627.

Zhou, C., and T. Li, 2010: Upscale feedback of tropical synoptic variability to intraseasonal oscillations through the nonlinear rectification of the surface latent heat flux. *J. Climate,* **23,** 5738–5754.